PHYSICAL REVIEW FLUIDS **3**, 083501 (2018)

Observation of a link between energy dissipation rate and oscillation frequency of the large-scale circulation in dry and moist Rayleigh-Bénard turbulence

Dennis Niedermeier,[*] Kelken Chang,[†] Will Cantrell, Kamal Kant Chandrakar,
David Ciochetto,[‡] and Raymond A. Shaw[§]
Department of Physics and Atmospheric Sciences Program, Michigan Technological University,
Houghton, Michigan 49931, USA

(Received 22 December 2017; published 15 August 2018)

In this study both the small- and large-scale flow properties of turbulent Rayleigh-Bénard convection are investigated. Experiments are carried out using the Π chamber (aspect ratio $\Gamma = 2$) for Rayleigh number range $\mathrm{Ra} \sim 10^8$–10^9 and Prandtl number $\mathrm{Pr} \approx 0.7$. Furthermore, experiments are run for dry and wet conditions, i.e., top and bottom surfaces of the chamber are dry and wet, respectively. For wet conditions we further distinguish between conditions with and without the presence of sodium chloride aerosol particles which, if supersaturated conditions are achieved, lead to cloud droplet formation. We therefore refer to these conditions as moist and cloudy, respectively. We see that the addition of water vapor influences the turbulent flow. In all cases, the turbulent kinetic energy dissipation rates increase with increasing temperature difference, but the slopes are different for wet and dry convection. We do not observe a clear difference between moist and cloudy convection due to low liquid water content. A similar lack of collapse with Ra is observed for the characteristic oscillations of the large-scale circulation. We observe that the first normalized characteristic oscillation frequency increased with increasing temperature difference, i.e., increasing Ra, for all conditions considered, but the slopes are different for wet and dry convection with again no clear difference between moist and cloudy convection. It turns out that the sloshing or torsional mode of the large-scale circulation and the turbulent flow or energy dissipation rate seem to be influenced by the same mechanism additional to the effect of buoyancy alone. These observational results provide supporting evidence that the large-scale circulation is insensitive to phase composition or interfacial physics and rather depends only on the strength of the turbulence.

DOI: 10.1103/PhysRevFluids.3.083501

I. INTRODUCTION

Turbulent buoyancy-driven convection is ubiquitous in natural and applied flows and is known for its high efficiency in transporting energy relative to molecular conduction. The question of how heat transport depends on the temperature difference (expressed as the dependence of the Nusselt number on the Rayleigh number) has proven rich in physical complexity even for the relatively simple geometry of confined Rayleigh-Bénard convection with aspect ratios of order unity [1,2]. An intriguing feature of such flows is the formation of a large-scale circulation (LSC), emerging

---

[*] Present address: Leibniz Institute for Tropospheric Research, 04318 Leipzig, Germany; niederm@tropos.de

[†] Present address: University of Gothenburg, 405 30 Gothenburg, Sweden.

[‡] Present address: DnA-Science and Engineering Associates, South Kingstown, RI 02852, USA.

[§] rashaw@mtu.edu

from what otherwise is a random turbulent background; it is sometimes referred to as the wind of turbulence. The circulation turns out to be crucial for the efficiency of heat transfer [3–5], and understanding the dynamical links between the large-scale coherent flow and the noise of small-scale turbulence has been a recent focus [6]. The LSC undergoes slow sloshing and torsional oscillations, which are observed in both temperature and velocity fields [7] and have a power-law dependence on the Rayleigh number [8]. It has been suggested that the velocity and oscillation of the LSC are coupled through the nonlinear term in the Navier-Stokes equation [6], so we can expect that this is a path for exploring possible connections between large- and small-scale (turbulence) properties.

We approach this problem from its relevance to one of the most familiar examples of buoyant convection, clouds formed when a supersaturated vapor is generated in the presence of condensation nuclei. Clouds have extremely large Reynolds numbers and are therefore turbulent. Turbulence, in turn, drives entrainment and mixing in clouds, leading to strong fluctuations in aerosol concentration, temperature, water vapor, and consequently supersaturation affecting cloud droplet activation, growth, and decay [9,10]. The associated phase transition processes of water in turn can feed back on the turbulent flow due to latent heat release [11]. In this study we examine convection with and without water vapor and cloud formation in the Π chamber, introduced by Chang *et al.* [12], to investigate possible connections between small-scale turbulence properties and oscillations in the LSC. The ability to measure both dry and moist or cloudy convection allows us to observe different circulation and turbulence properties for the same temperature gradient, thereby providing a way to separate the dependence of turbulence properties on Rayleigh number versus LSC properties. Note, however, that the term "moist convection" is not used in the sense of large-scale atmospheric convection as factors, e.g., lapse rate, which strongly influence atmospheric convection cannot be represented in the Π chamber.

Turbulence is created via a temperature difference between the top and bottom surfaces inside the chamber, inducing turbulent Rayleigh-Bénard (RB) convection. In our study different temperature differences between the top and bottom surfaces are set while the mean temperature stays constant. Experiments are run for dry and wet conditions, i.e., top and bottom surfaces are dry and wet, respectively. For wet conditions we further distinguish between conditions with and without the presence of sodium chloride aerosol particles which, if supersaturated conditions are achieved, lead to cloud droplet formation. We therefore will refer to these conditions as moist and cloudy, respectively. In the cloudy case, for example, cloud droplets are continuously activating and growing as well as evaporating during the turbulent mixing. We restrict the current study to temperature gradients and accompanying supersaturations that produce cloudy liquid water mixing ratios sufficiently small that latent heating effects and direct coupling of droplets to the flow can be neglected.

The paper is structured as follows. We introduce the experimental approach and provide some initial characterization of dry versus wet turbulent convection in Sec. II. Then the buoyancy and Rayleigh number for dry, moist, and cloudy convection are briefly described in Sec. III for completeness. Section IV is focused on measurements of the small-scale turbulence and Sec. V on the LSC. That section continues by considering how small and large scales are related. Results are summarized and the paper is concluded in Sec. VI.

II. EXPERIMENTAL APPROACH AND CHARACTERIZATION OF DRY AND WET TURBULENT CONVECTION

The Π chamber used for the experiments is introduced briefly, and more detailed information is given by Chang *et al.* [12]. Within the Π chamber, atmospherically relevant cloud conditions can be achieved (e.g., pressures ranging from surface values of 1000 hPa down to about 60 hPa, and temperatures of $-55\,^{\circ}\mathrm{C}$ to $+55\,^{\circ}\mathrm{C}$). The chamber is of rectangular shape with an internal volume available for experiments of about 5 m^3. In this study this volume is reduced to 3.14 m^3 by installing a cylindrical thermal panel (1-m height H, 2-m diameter D, leading to an aspect ratio $D/H \equiv \Gamma = 2$). A schematic view of the chamber and cylindrical panel is shown in Fig. 1. The thermal panels, regulating the temperature within the chamber, are controlled on three separate circuits,

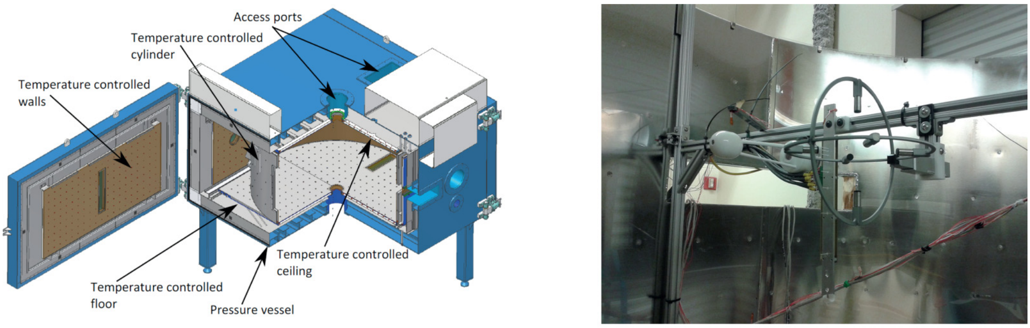

(a)

(b)

FIG. 1. (a) Sketch of the cloud chamber with one door being open and the cylindrical thermal panel being in place [12]. (b) Picture of the instrumentation inside the cylinder. The IR absorption hygrometer, the sonic anemometer, and the thermistor array were placed such that the distance between the instruments is as small as possible in order to avoid cross influence between the instruments but to ensure possible cross correlations.

corresponding to the top, bottom, and the sidewall sections of the chamber internal workspace. The cylindrical sidewall has an acrylic liner to minimize thermal conduction between the wall and the fluid.

Turbulence is induced through RB convection by heating the bottom surface and cooling the top surface inside the chamber. In this study three different setups are investigated. In the first case all boundaries are dry; we will refer to this as dry convection. In the second and third cases the top and bottom boundaries are wet by covering both surfaces with glass fiber filter paper (Type A/E Glass Fiber, Pall Corporation, Ann Arbor, MI, USA) and connecting these to water reservoirs to ensure long-lifetime liquid boundaries. In the second case, which we will refer to as moist convection, the chamber contains given concentrations of water vapor depending on the temperature difference between the top and bottom surfaces, but due to the absence of cloud condensation nuclei (CCN), no condensed liquid water in terms of cloud droplets is present. In the third case, sodium chloride particles are fed into the chamber. These particles are generated by atomizing aqueous solutions of 1 g of salt per one liter of deionized water. The resulting aerosol particles are dried in a diffusion dryer and the resulting whole particle distribution (mean diameter of about 50 nm, number concentration of about $2 \times 10^6\ \mathrm{cm}^{-3}$) is then added to the chamber at a flow rate of 2 l/min. Due to the large chamber inner volume, the mean particle number concentration inside the chamber is about $1200\ \mathrm{cm}^{-3}$. If the conditions are appropriate inside the chamber (i.e., reaching supersaturation conditions) the NaCl particles can act as CCN activating to cloud droplets. Therefore, we are referring to cloudy convection in this case.

All experiments presented here are made in air at ambient pressure (about 1000 hPa). Different gradients are set while the mean temperature stays constant. The temperature of the wall is set to $T_0 = 10\,^\circ\mathrm{C}$. The temperatures of the top and bottom surfaces are set to $T_{\mathrm{top}} = T_0 - \frac{1}{2}\Delta T$ and $T_{\mathrm{bottom}} = T_0 + \frac{1}{2}\Delta T$, respectively, with $\Delta T = 2$, 4, 6, 8, and 10 K for dry boundaries and $\Delta T = 2$, 4, 6, and 8 K for moist and cloudy convection experiments.

The Rayleigh number Ra is on the order of 10^8–10^9 (discussed below) for the set boundary conditions and the chamber height of 1 m. The Prandtl number Pr is about 0.72 for dry convection and 0.67 for wet convection (that includes both moist and cloudy convection). For each gradient steady-state turbulent (cloudy) conditions are sustained for times of about 8 h to several days.

In the experiments an IR absorption hygrometer (LI-7500 open path H_2O gas analyzer, LI-COR®), a sonic anemometer (V probe; Applied Technologies, Inc.), eight resistance thermometers [resistance temperature detectors (RTDs), Minco], and a thermistor array consisting of eight thermistors (Honeywell 111-104HAK-H01) are used to characterize the thermodynamic variables as well as turbulent air motion inside the chamber. The suite of instruments is shown in Fig. 1(b). The

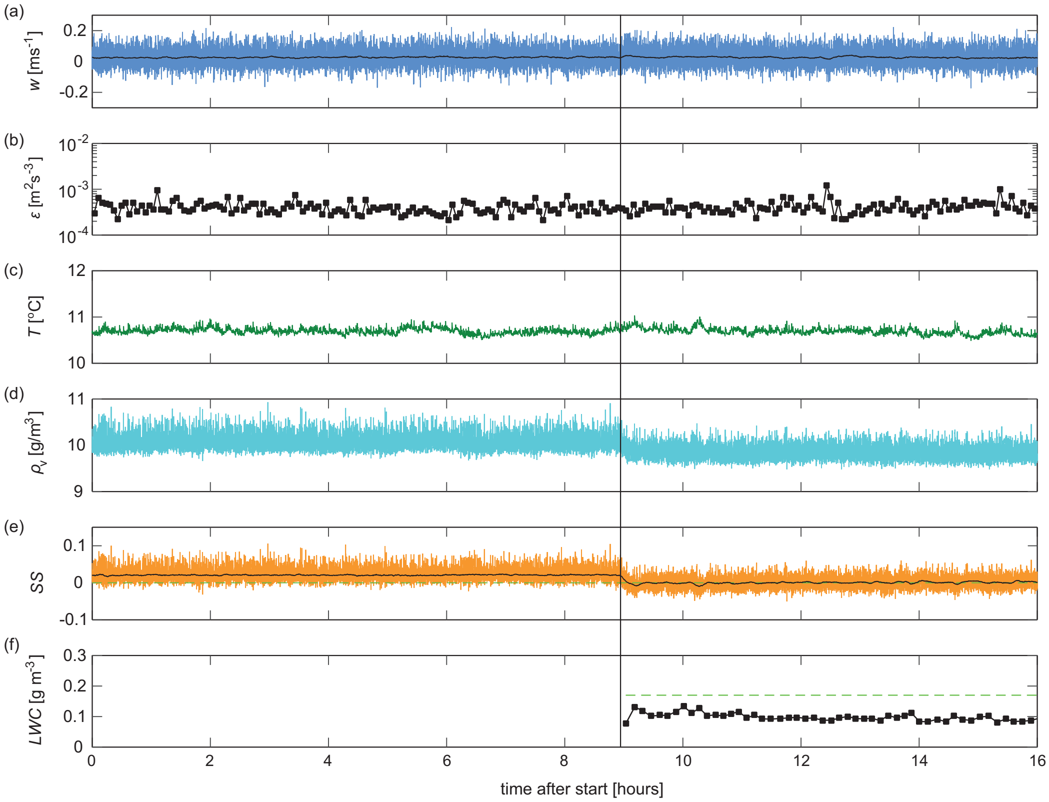

FIG. 2. (a) Vertical velocity plus running mean, (b) kinetic energy dissipation rate (4 min average), (c) temperature measured in the center of the chamber, (d) water vapor mass density, (e) supersaturation based on the water vapor partial pressure (H_2O analyzer measurements) and the saturation vapor pressure (based on the RTD closest to the H_2O analyzer), and (f) LWC based on PDI data (black squares) and based on the water vapor concentration difference before and after cloud formation (dashed green line).

hygrometer and the sonic anemometer are positioned at the midheight of the chamber. The horizontal distance between the hygrometer and the sonic anemometer is about 20 cm, while the hygrometer is about 45 cm away from the wall. The RTDs are situated at various spots inside the chamber, with two of them being very close to the hygrometer. The thermistor array is positioned in between the hygrometer and the sonic anemometer with the first thermistor (position 0 mm) being at same height as the hygrometer. Two out of eight thermistors quit working during the experiments. At the end six thermistors are available for evaluation with separations compared to the very first thermistor of 0, 5.0, 12.8, 25.0, 43.9, and 191.0 mm. Cloud droplet sizes and motions are recorded with the phase Doppler interferometer (PDI) (Dantec Dynamics). The measuring volume of the PDI is approximately 30 cm away from the bottom and sidewall.

Figure 2 shows an example of measurements obtained during a wet convection experiment for $\Delta T = 8$ K. This experiment generated steady-state conditions for about 24 h. For about the first 9 h of the run the chamber was moist i.e., no aerosol particles were inside the chamber. Then we introduced particles at a chamber-averaged aerosol injection rate of about 1200 $\text{cm}^{-3}\,\text{min}^{-1}$. Figure 2(a) depicts the vertical velocity component measured by the sonic anemometer at 20 Hz. It can be observed that the mean vertical velocity is close to zero, while the fluctuations are up to 0.2 m/s. Based on second-order kinetic energy structure function and applying the elliptic model (details are given in Sec. IV), the turbulent kinetic energy dissipation rate, averaged over a time interval of 4 min, was calculated as a measure of turbulence degree inside the chamber [Fig. 2(b)]. Figure 2(c) shows the temperature measured in the center of the chamber by an RTD at 1 Hz. It can be determined from these measurements that the convection is indeed stationary in time. Furthermore, for all three variables, i.e., velocity, dissipation rate, and temperature, we do not observe a significant difference between moist and cloudy convection, thereby confirming that liquid water contents are sufficiently low that thermodynamic and mechanical influences on the flow can be neglected even for the largest temperature difference. In contrast, a significant change can be observed in the water vapor density and supersaturation data depicted in Figs. 2(c) and 2(d). Water vapor density is based on the H_2O analyzer measurements performed at 20 Hz. The partial water vapor pressure has been calculated, which together with the saturation vapor pressure (based on the RTD measurements closest to the H_2O analyzer) is applied to derive supersaturation inside the chamber. Fluctuations in temperature and in water vapor concentration lead to a randomly, strongly varying supersaturation. The mean supersaturation is approximately 2% in the moist case. As soon as aerosol injection starts, the supersaturation decreases and reaches zero, on average, showing that the NaCl particles act as CCN.

This behavior is further confirmed through the liquid water content (LWC) derived from the PDI measurements, which is above zero as soon as the particle injection starts [Fig. 2(f)]. On average, the LWC is about 0.1 $\mathrm{g/cm^3}$. We also calculated a mean LWC based on the vapor concentration difference between moist and cloudy convection, assuming that the reduction in water vapor (i.e., supersaturation) is due to droplet activation and growth. It is about 0.17 $\mathrm{g/cm^3}$, i.e., it agrees within a factor of 2 with the LWC based on the PDI data. How water vapor and liquid water content can influence the buoyancy and the Rayleigh number is considered in the next section.

III. BUOYANCY AND RAYLEIGH NUMBER FOR DRY, MOIST, AND CLOUDY AIR

Because both small- and large-scale properties have been observed to exhibit power-law scaling with Rayleigh number, we briefly describe buoyancy and Rayleigh number for dry and moist convection. The buoyancy for dry convection can be approximated as

$$B_d = \frac{T - T_0}{T_0} g, \tag{1}$$

where T is the temperature of the air parcel, T_0 is the temperature of the surrounding environment, and g is the gravitational acceleration. The buoyancy for moist convection can be approximated as [13]

$$B_v = \frac{T_v - T_{v,0}}{T_{v,0}} g, \tag{2}$$

where the virtual temperature is defined as $T_v = T(1 + \epsilon q_v)$, with q_v being the water vapor mixing ratio, which we obtain from the hygrometer measurements and $\epsilon = m_d/m_v - 1$; here m_d is the molecular mass of dry air and m_v is the molecular mass of water. Finally, the buoyancy for convection with water vapor and condensed liquid water can be written as

$$B_l = \left(\frac{T_l - T_{l,0}}{T_{l,0}} - q_l \right) g, \tag{3}$$

where the liquid water temperature T_l is the temperature that would exist if all liquid water were evaporated [14,15]:

$$T_l = T \exp\left(-\frac{L q_l}{c_p T} \right) \approx T - \frac{L}{c_p} q_l; \tag{4}$$

here q_l is the liquid water mixing ratio, L is the latent heat of vaporization, and c_p is the specific heat of air at constant pressure. We note that since the experiments are run at atmospheric pressure Eq. (4) is written in terms of temperature rather than potential temperature. Finally, in Eq. (3) the

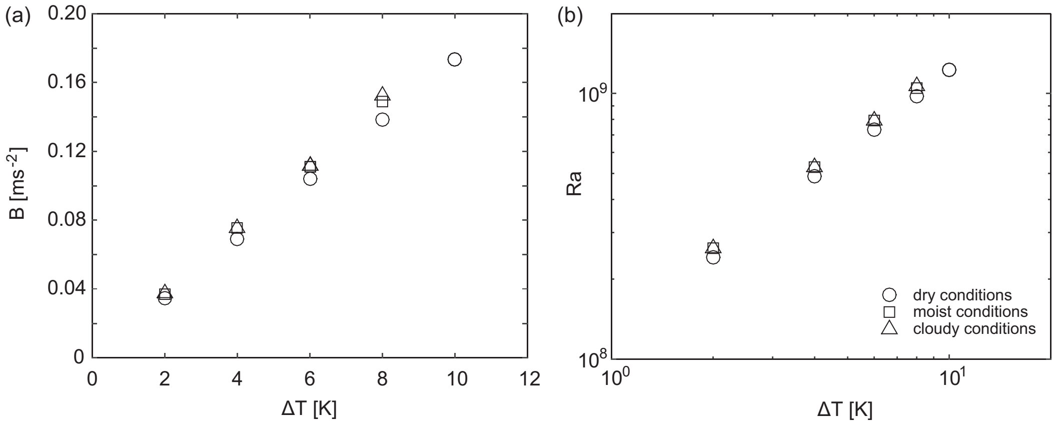

FIG. 3. (a) Buoyancy as a function of temperature difference for all conditions investigated. (b) Rayleigh number as a function of temperature difference for all conditions investigated.

subtracted q_l term comes from the liquid water drag due to droplet settling. In our experiments, q_l is determined from the PDI measurements.

In Fig. 3(a), buoyancy is shown as a function of temperature difference for the different conditions. Buoyancy increases as expected with increasing temperature difference. For moist conditions the buoyancy is higher than for dry convection and the difference between both increases with increasing ΔT since the amount of water vapor also increases with increasing ΔT. The additional presence of cloud droplets is not visible for the two lowest ΔT's investigated but becomes visible, albeit minimally, for the two highest temperature differences considered. For $\Delta T = 2$ and 4 K, the LWC is less than 0.01 g m^{-3}. For $\Delta T = 6$ and 8 K it is about 0.02 and 0.10 g m^{-3}, which explains the weak differences between moist and cloudy convection.

As mentioned above, the buoyancy force is opposed by viscous damping in the fluid. Furthermore, thermal diffusion causes the rising (hot) fluid parcel to equilibrate with the surrounding fluid leading to a destruction of the buoyant force. The competition of the buoyancy force with viscous drag and thermal diffusion is summarized by the dimensionless Rayleigh number Ra. For dry convection the Rayleigh number can be written as

$$\mathrm{Ra}_d = \frac{g \Delta T H^3}{T_0 \nu \kappa_T}, \tag{5}$$

where H is the distance between the warm and cold boundaries, ν is the kinematic viscosity, and κ_T is the thermal diffusivity. When water vapor is included for moist convection this can be written as

$$\mathrm{Ra}_v = \frac{g \Delta T H^3}{T_0 \nu \kappa_T} + \frac{g \epsilon \Delta q_v H^3}{\nu \kappa_T}. \tag{6}$$

A detailed derivation of Eq. (6) is given in the Appendix. For cloudy convection, i.e., when cloud droplets are present, another, cloudy Rayleigh number Ra_c needs to be formulated. However, we have seen that the presence of cloud droplets does not significantly change the buoyancy term. Due to that, we use the same expression for Ra as used in the moist convection case ($\mathrm{Ra}_c = \mathrm{Ra}_v$) and we will leave an exact expression of Ra_c to future studies.

In Fig. 3(b), Ra is shown as a function of temperature difference for the different conditions. Similar to the buoyancy case, Ra increases as expected with increasing temperature difference. For moist and cloudy conditions Ra is higher than for dry convection and the difference between both increases with increasing ΔT since the amount of water vapor also increases with increasing ΔT.

IV. DISSIPATION RATE DETERMINATION

In this section we present the observations of small-scale turbulence, focusing on the turbulent kinetic energy dissipation rate (Sec. IV B). Because of the lack of a large mean flow and the corresponding difficulty in using the standard Taylor frozen-flow approach, we begin by discussing our use of the elliptic model to obtain estimates of the dissipation rate in Sec. IV A.

A. Elliptic model for dissipation rate calculation

To obtain the turbulent kinetic energy dissipation rate of the bulk fluid in Rayleigh-Bénard convection we use the velocity space-time cross-correlation function

$$C_v(r,\tau) = \langle v(x+r,t+\tau)v(x,t)\rangle_t/[(\sigma_v)_1(\sigma_v)_2], \tag{7}$$

where v represents the velocity fluctuations and $(\sigma_v)_i$ is the respective rms value at position i [16–18]. In experimental studies of large-scale flows such as wind tunnel experiments or atmospheric measurements, time-domain measurements play a major role. In order to transfer the collected time-domain results into space-domain results, Taylor's frozen-flow hypothesis is usually applied assuming that turbulent fluctuations in space do not significantly change while being carried through a fixed location by a large mean flow U_0, i.e., U_0 has to be much larger than the velocity fluctuations σ_v. In terms of the cross-correlation function, this means $C_v(r,\tau) = C_v(r_T,0)$ with $r_T = r - U_0\tau$. However, for RB convection σ_v is of the same order as or even larger than U_0, so the conditions of Taylor's frozen-flow hypothesis are not met.

He and Zhang [16] proposed a model where $C_v(r,\tau)$ has a scaling form $C_v(r_E,0)$ with r_E being of elliptical shape:

$$r_E^2 = (r - U\tau)^2 + V^2\tau^2. \tag{8}$$

Here U is a characteristic convection velocity proportional to U_0 and V is associated with a random sweeping velocity, proportional to σ_v. Note that for $V = 0$, $r_E = r_T$.

In order to determine the scaling form in our experiments we need spatial and temporal information for the flow. Here we note that in the bulk region of the flow (the region where our measurements were performed), temperature is a passive scalar. That means the temperature field is mixed due to the turbulent motion [19] and in consequence velocity and temperature fluctuations share the same decorrelation mechanism [20]. So it is expected that $C_T(r,\tau)$ and $C_v(r,\tau)$ have roughly the same scaling form [17]

$$C_T(r,\tau) = \langle \delta T(x+r,t+\tau)\delta T(x,t)\rangle_t/(\sigma_T)_1(\sigma_T)_2, \tag{9}$$

where δT represents the temperature fluctuations and $(\sigma_T)_i$ is the respective rms value at position i. We will use data provided by the thermistor array (measured at 20 Hz) to determine U and V. As mentioned earlier, the thermistor array consists of six properly functioning thermistors with separations from the very first sensor of 0 mm, 0.5 cm, 1.3 cm, 2.5 cm, 4.4 cm, and 19.1 cm. We did the analysis two times: first using all six sensors and second excluding the last sensor, i.e., the one being 19.1 cm away from the first sensor because the data suggest that 19.1 cm is greater than the large-eddy correlation length. The determined kinetic energy dissipation rates of both methods agree within a factor of 1.5–2, which is well within the variability of the 4-min average of the kinetic energy dissipation rate as shown in Fig. 2. Here we only present results using the first five sensors for our analysis.

The resulting isocorrelation contours of $C_T(r,\tau)$ (not shown) emerge as a set of elliptical curves having similar orientation and aspect ratio. These are determined by the scaling velocities U and V, which can be obtained from the measured $C_T(r,\tau)$. Figure 4 shows the measured peak position τ_p as a function of r (shown for the moist convection experiment at $\Delta T = 8$ K, as a specific example), which can be fitted by a linear function $\tau_p = \alpha r$, with $\alpha = U/(U^2 + V^2) = 8 \times 10^{-3}$ s mm^{-1}. Similarly we can obtain the peak position r_p from the $C_T(r,\tau)$ versus r curve at fixed τ [17]: $r_p = U\tau$, with

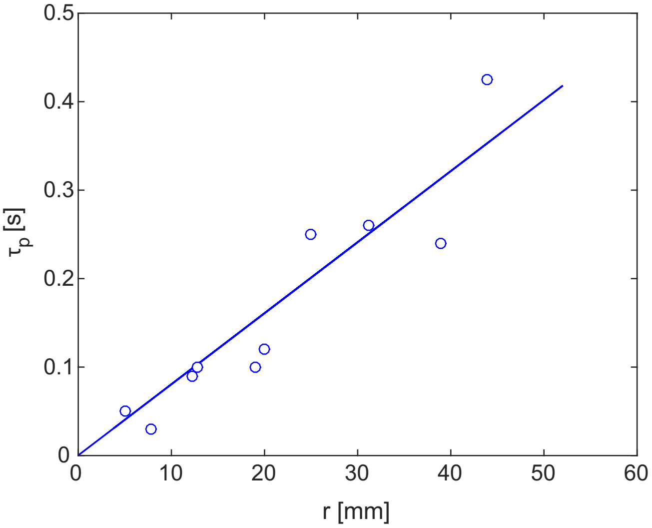

FIG. 4. Peak position τ_p as a function of r. The dotted line shows the fitted function $\tau_p = \alpha r$, with $\alpha = 7.9\times10^{-3}$ s mm^{-1}.

$U = 2$ mm s^{-1} (not shown). With these values we determine $V = 15$ mm s^{-1}. The rms velocity σ_u based on the sonic data is, for this particular case, 34 mm s^{-1}, i.e., a factor of 2 larger than V but still comparable to V.

B. Dissipation rates

An important implication from Eq. (8) is that for $r = 0$, we can obtain $r_E = (U^2 + V^2)^{1/2}\tau$. This is used to first calculate the average bulk kinetic energy dissipation rate $\varepsilon_{\text{bulk}}$ assuming that the scaling is also valid for the vertical velocity component obtained from the sonic anemometer, which is situated about 10 cm away from the thermistor array. We used the second-order velocity structure function

$$S_w(r_E) = \langle [w(x,t) - w(x + r_E, t)]^2 \rangle = C_1 \varepsilon_{\text{bulk}}^{2/3} r_E^{2/3}, \tag{10}$$

where $\langle\cdot\rangle$ denotes the spatial average and $C_1 = 2.1$ is the Kolmogorov constant. In Fig. 5, the obtained structure function is exemplarily shown for a moist convection experiment for $\Delta T = 8$ K, displaying a clear $r_E^{2/3}$ regime. Finally, the average bulk thermal dissipation rate $\varepsilon_{T,\text{bulk}}$ has also been determined by applying the second-order temperature structure function

$$S_T(r_E) = \langle [\delta T(x,t) - \delta T(x + r_E, t)]^2 \rangle = 4.02 C_\theta \varepsilon_{T,\text{bulk}} \varepsilon_{\text{bulk}}^{-1/3} r_E^{2/3}, \tag{11}$$

with C_θ being the Obukhov-Corrsin constant, which is close to 0.4 based on laboratory data [21,22].

The determined thermal and kinetic energy dissipation rates for the bulk fluid (i.e., away from the boundary layers) are shown in Fig. 6 as a function of temperature difference and as a function of Ra. It can be observed that dissipation rates increase with increasing temperature difference but the slopes are different for wet and dry convection. Also, as anticipated for the low q_l observed in these experiments, we do not observe a significant difference between moist and cloudy convection. The lack of collapse to a single line in the $\varepsilon_{\text{bulk}}$ vs Ra plot suggests that the modified Rayleigh numbers presented in Sec. III do not capture the full difference in the experiments. We speculate that this difference arises from one of two sources. One could be the slightly different texture of the boundary layer: The filter paper used in the wet experiments may change the boundary layer roughness. If we think of the temperature profile in the chamber as an S curve, with somewhat higher gradients

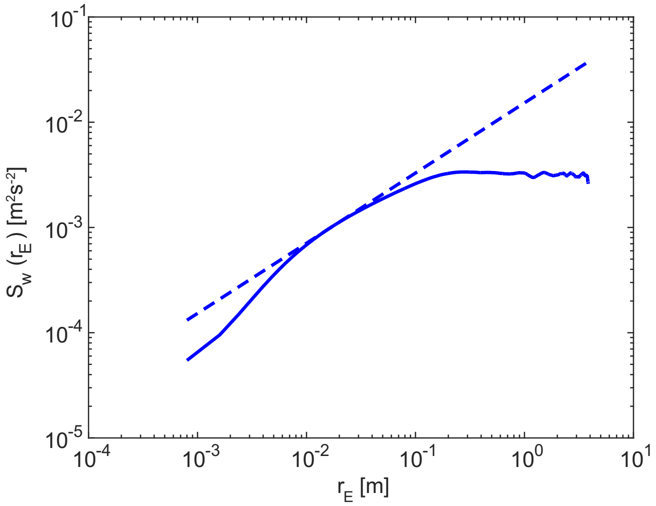

FIG. 5. Second-order velocity structure function (solid line) including the $r_E^{2/3}$ fit (dashed line) for the $\Delta T = 8$ K moist convection case.

near the boundaries and weaker gradients in the center, the dissipation rate in the bulk fluid should basically be related to the slope of the S curve in the center. If the boundary layers are changing differently between dry and moist convection, then the dry vs moist S curves could be also changing differently. The other possible source is that, in a supersaturated flow, there will be condensation onto the sidewalls of the chamber, resulting in a small latent heat flux into the fluid near the sidewalls. We favor the first explanation, since the difference between the dry and wet observations decreases with increasing water vapor supersaturation (i.e., with increasing ΔT). That small features of the walls could detectably influence the turbulence properties is perhaps not surprising given that for our range of Ra and Pr there exist different flow regimes in which the globally averaged dissipation rate can change from boundary dominated to bulk dominated [1,2], as discussed further below. In either

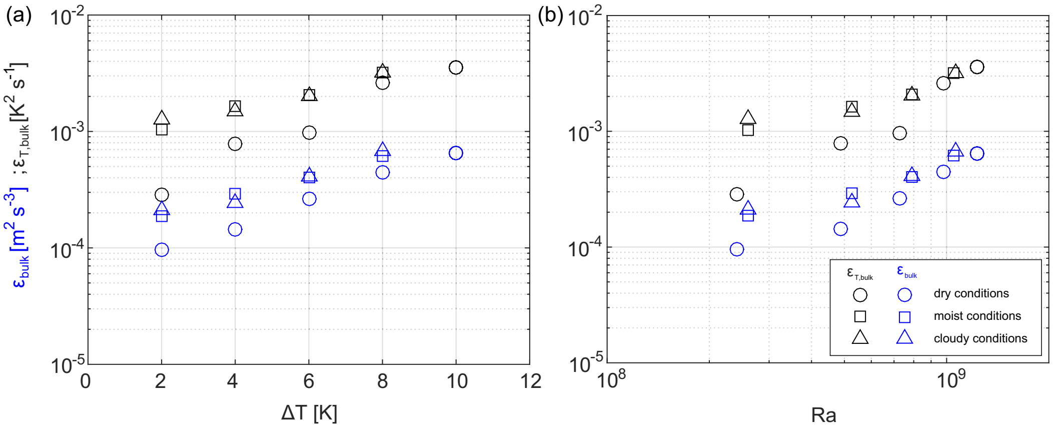

FIG. 6. Thermal and kinetic energy dissipation rate as a function of (a) temperature difference and (b) Ra. Dissipation rates are based on second-order structure function calculated from the vertical velocity component as measured by the sonic anemometer and calculated from the temperature data obtained from the thermistor array. The elliptic model has been applied since the mean velocity is on the same order as the rms value.

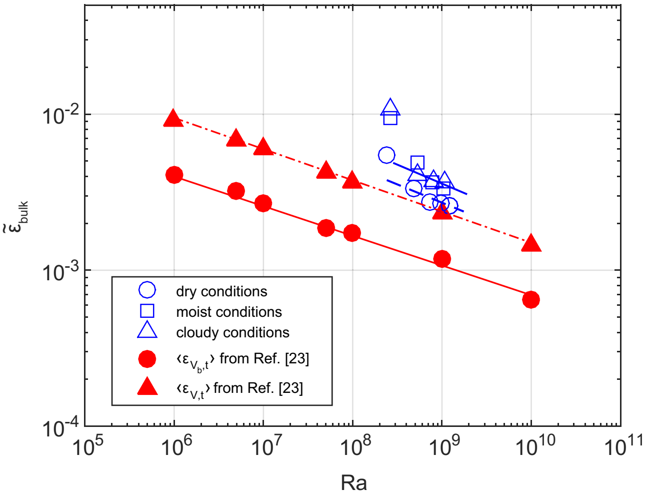

FIG. 7. Dimensionless kinetic energy dissipation rate $\tilde{\varepsilon}_{\text{bulk}}$ as a function of Ra. For comparison, dissipation rates determined by Scheel and Schumacher [23] obtained for their full cylinder volume V (red closed triangles) and a subvolume V_b (red closed circles) are presented too. Scaling laws were fitted to the data; determined exponents are given in the text.

case, the origin is not critical for the study, but rather provides an opportunity to obtain different turbulence properties even for the same ΔT, as originally intended. Eventually, this aspect will be used in the comparison to observations of the LSC and its dependence on ΔT.

In Fig. 7 the dimensionless kinetic energy dissipation rate $\tilde{\varepsilon}_{\text{bulk}} = \varepsilon_{\text{bulk}} H/U_{\text{f}}^3$ is plotted as a function of Ra in comparison to data obtained by Scheel and Schumacher [23] (Pr = 0.7). The chamber height H and the free-fall velocity given through $U_{\text{f}} = \sqrt{g\alpha\Delta T H}$ [2] are used to obtain $\tilde{\varepsilon}_{\text{bulk}}$, with α being the thermal expansion coefficient. Scheel and Schumacher [23] showed two different curves, the first one obtained in their full cylinder volume V, the second one obtained for a subvolume V_b centered in the bulk away from all walls. It can be observed in Fig. 7 that our determined dimensionless kinetic energy dissipation rates are higher than those of Scheel and Schumacher [23]. The reason is that the prefactor in the scaling law $c_\tau = a\,\text{Ra}^b$ usually depends on the experiment and is not universal. For example, in our experiments the aspect ratio is $\Gamma = 2$, while in [23] it is $\Gamma = 1$. The amplitude also depends on the size of the bulk volume V_b. Fitting the scaling law c_τ without the $\tilde{\varepsilon}_{\text{bulk}}$ values for lowest Ra, we obtain $b = -0.23 \pm 0.1$ (dry convection) and $b = -0.25 \pm 0.1$ (moist and cloudy convection), which agrees well with those values for b obtained by Scheel and Schumacher [23] ($b = -0.20 \pm 0.01$ for the full cylinder volume V and $b = -0.19 \pm 0.01$ for subvolume V_b).

Dissipation occurs in both the boundary layer (BL) and the bulk. The central idea of the Grossmann-Lohse theory [24–27] is that the global kinetic energy and thermal dissipation rates $\varepsilon_{\text{global}}$ and $\varepsilon_{T,\text{global}}$ can be split into the BL and bulk contributions

$$\varepsilon_{\text{global}} = \varepsilon_{\text{BL}} + \varepsilon_{\text{bulk}}, \tag{12}$$

$$\varepsilon_{T,\text{global}} = \varepsilon_{T,\text{BL}} + \varepsilon_{T,\text{bulk}}. \tag{13}$$

With our method we only determined the bulk contributions. In Fig. 3 of Ahlers *et al.* [1], four main regimes in parameter space are shown, which are characterized by different contributions of ε_{BL}, $\varepsilon_{T,\text{BL}}$, $\varepsilon_{\text{bulk}}$, and $\varepsilon_{T,\text{bulk}}$ to the respective global dissipation rates $\varepsilon_{\text{global}}$ and $\varepsilon_{T,\text{global}}$. In our case, the Prandtl number is ~0.72 for dry convection and ~0.67 for wet convection with Ra ~ 10^8–10^9; i.e., our measurements go from regime II to regime IV. In both regimes the global kinetic energy

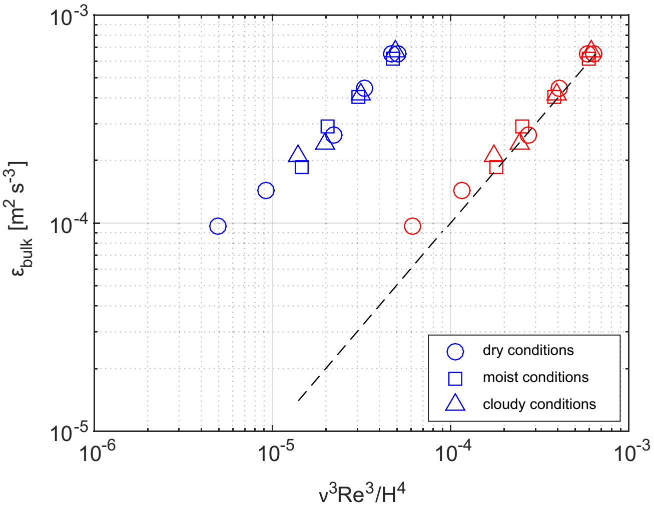

FIG. 8. Average kinetic energy dissipation rate of the bulk as a function of bulk scaling according to, e.g., Chillà and Schumacher [2]. For the blue symbols, H is the height of the Π chamber, which is 1 m. The dashed line represents the 1:1 line. In order to obtain the 1:1 fit, H has to be decreased to 0.08 m, which corresponds to the integral length l (red symbols). A scaling with Re^3 was also obtained in [23] for $\mathrm{Pr} = 0.7$ and Ra between 10^6 and 10^{10}, which also showed that the kinetic energy dissipation rate in the bulk dominates.

dissipation rates are dominated by the bulk contributions. (Data of Scheel and Schumacher [23] for $\mathrm{Pr} = 0.7$ and Ra between 10^6 and 10^{10} also show that kinetic energy dissipation in the bulk dominates.) However, the global thermal dissipation rates are dominated by the BL contribution for $\mathrm{Ra} < (2\text{–}3) \times 10^8$ and bulk dominated for higher Ra.

Now that we have formed a picture of the small-scale turbulence and its dependence on Ra, we begin to turn our attention to its relationship to the large-scale flow properties. From Kolmogorov's energy-cascade picture [1], the average bulk energy dissipation rate scales with

$$\varepsilon_{\mathrm{bulk}} \sim \frac{U^3}{H} = \frac{\nu^3}{H^4}\mathrm{Re}^3, \tag{14}$$

with U being the mean large-scale velocity near the boundaries of the cell. In addition, H is the height of the chamber and $\mathrm{Re} = UH/\nu$ is the Reynolds number. We show how the measured ε scales with this estimate in Fig. 8. Grossmann and Lohse [24–27] argue that the relevant velocity scale is the wind of turbulence U being associated with the LSC and not the velocity fluctuations σ_u (which originate from the large-scale coherent flow with velocity U) because it is U which stirs the fluid in the bulk. On the other hand, Chillà and Schumacher [2] state that the characteristic velocity U in Eq. (14) is, for example, a rms velocity probing the large-scale turbulence (and thus the wind) in the system. In Fig. 8 we used σ_u instead of the mean wind U (which we did not measure because of the position of the sonic anemometer with the smallest distance to the sidewall being about 65 cm). It can be seen that the scaling (1:1 line match) is present only if H is set smaller than the height of the chamber. It has to be decreased to 0.08 m, which corresponds to the integral length scale l, which is based on the autocorrelation of the vertical velocity fluctuations and using $r_E = (U^2 + V^2)^{1/2}\tau$ in order to convert from time to space. Regardless of which scale is used, we see evidence suggesting that the small-scale turbulence observations exhibit a close linkage with the large-scale flow properties (even when not showing a simple dependence on Ra for the dry versus wet conditions).

A final note is in order before continuing with another fascinating feature of RB convection: We deliberately do not report on Nusselt numbers Nu in the context of this paper because (a) we do not have a direct measurement of Nu, (b) we only measure bulk properties, but are at the edge of the

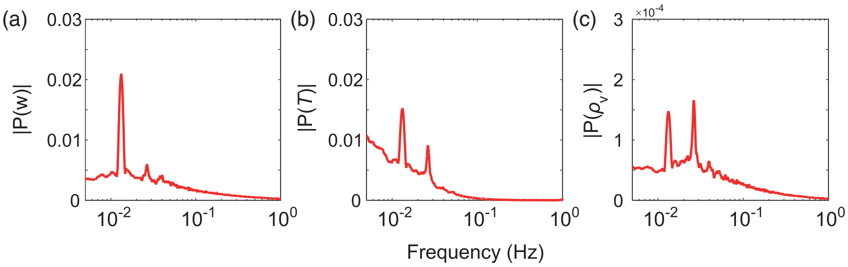

FIG. 9. (a) Frequency power spectra of the w component, (b) T measured close to the H_2O analyzer, and (c) raw water vapor absorptance for the wet RB convection experiment ($T_0 = 10\,^\circ\mathrm{C}$ and $\Delta T = 8$ K). The prominent peak near $f_0 = 0.013$ Hz corresponds to similar oscillation frequencies (for the same Ra) measured in previous studies (see [7]).

bulk- and BL-dominated global thermal dissipation rate, and (c) the focus of this paper is on the connection between LSC and the turbulence as further pursued in the next section. Therefore, a full characterization of the Nu numbers will be a topic for continued research.

V. LARGE-SCALE CIRCULATION: COHERENT OSCILLATIONS

A fascinating feature of RB convection is the presence of coherent oscillations observed in both velocity and temperature fields, for different convection aspect ratios and different fluids (see, e.g., [1] and references therein). As mentioned already, the LSC is essentially the organized circulation known as the wind of turbulence and its oscillations can be considered as one of its main characteristics. Figure 9 shows frequency power spectra for velocity, temperature, and water vapor concentration, for moist convection with $\Delta T = 8$ K. The measurements were made in the bulk of the fluid at the midheight of the chamber. We observe characteristic frequencies in the velocity and temperature field, but also in the water vapor data. Interestingly, the prominent peak in the velocity and temperature data is at $f_0 = 0.013$ Hz, which corresponds to similar oscillation frequencies (for the same Ra) measured in previous studies (see [7] and references therein). There is a second peak clearly visible at $2f_0$, which interestingly is the most prominent peak in the water vapor data. We observed these characteristics for all temperature differences investigated. Since the sensor positions are fixed during the experiments, these determined characteristic frequencies should not be caused by the simple turnover of the LSC.

It has been observed for cylindrical samples with $\Gamma = 1$ that the rotational invariance of the cell gets broken by the LSC plane, leading to oscillations of the circulation plane (see, e.g., [1,8,28–36]). It has been suggested that the observed oscillations are caused by a torsional motion of the LSC in which the orientation of the upper half of the LSC undergoes azimuthal oscillations [3,36] being out of phase with those of the lower half [1,3,37,38]. Xi *et al.* [7] showed through multiple temperature measurements at the bottom, at the top, and at the midheight of a cylindrical convection cell ($\Gamma = 1$) filled with water that the prominent peak at f_0 is caused by an off-center (azimuthal) oscillation or "sloshing" mode of the velocity field in the bulk fluid. That means there is a horizontal oscillation of the bulk fluid along the direction perpendicular to the vertical plane of the LSC. Indications of this sloshing mode have already been observed by Qiu *et al.* [8], who showed in an earlier study that the strongest oscillation occurred in the direction perpendicular to the LSC plane. Within one period of the off-center motion the central line of the LSC seems to cross the sensor plane, i.e., the plane where our sensors are situated, twice, which leads to the peak at $2f_0$ [7]. Finally, Xi *et al.* [7] concluded from their experimental observations that thermal plumes are emitted neither periodically nor alternately from the top and bottom plates and that temperature oscillations are caused by the sloshing mode and the torsional mode of the velocity field in the central and BL regions of the system, respectively. In this context, Brown and Ahlers [39] explained theoretically the origin of both modes, saying that oscillations seen in some of the local temperature measurements are caused

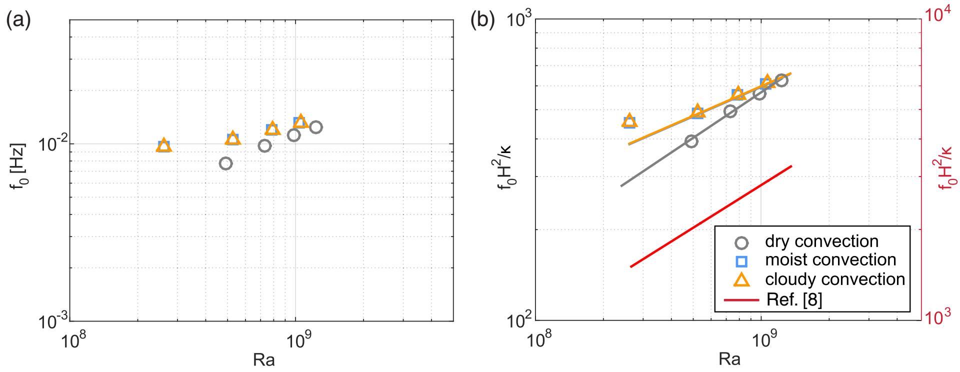

FIG. 10. (a) Oscillation frequency f_0 and (b) normalized oscillation frequency $f_0 H^2/\kappa$ for different temperature gradients (i.e., different Rayleigh numbers). Here H is the chamber height and κ is the thermal diffusivity of air or the diffusivity of water vapor in air. The solid lines in (b) represent power-law fits (dry convection, $f_0 H^2/\kappa = 0.017\,\mathrm{Ra}^{0.50}$; wet convection, $f_0 H^2/\kappa = 0.636\,\mathrm{Ra}^{0.33}$). The red line represents the power-law fit determined by Qiu *et al.* [8] for RB convection experiments in water ($f_0 H^2/\kappa = 0.167\,\mathrm{Ra}^{0.47}$).

by the sloshing mode and not by periodic plume emission from the thermal boundary layers. Periodic oscillations of both temperature and velocity have also been observed for cylindrical samples with $\Gamma = 2$, e.g., in mercury with $\mathrm{Pr} = 0.024$ [40].

What is intriguing in our experiments is that we observe a clear difference in f_0 and consequentially in $2f_0$ between dry and wet convection for a given ΔT and Ra, respectively (see Fig. 10). First of all, f_0 increases with increasing temperature difference, i.e., increasing Ra, for all conditions, but the slopes are different for wet and dry convection. Second, we do not observe a clear difference between moist and cloudy convection. The question arises whether an asymmetry in the up- and downwelling velocity is present which could provide an explanation for these results. For both dry and wet convection we do not observe a distinct asymmetry in the up- and downdrafts. In general, factors (e.g., lapse rate) which strongly influence atmospheric convection cannot be represented in the Π chamber. Release of latent heat in the chamber experiments is based on turbulent mixing, not on positive vertical velocity as in the atmosphere. In other words, the existence of a lapse rate and associated adiabatic cooling with vertical motion is negligible in these experiments. Therefore, the asymmetry known to be a defining feature of large-scale atmospheric moist convection (e.g., [41,42]) is not observed in our experiments.

In Fig. 10(b), the corresponding normalized oscillation frequency of the prominent peak f_0, i.e., $f_0 H^2/\kappa$, is plotted as a function of Ra. Note that no significant change in slope for the moist and wet convection cases occurs when we plot the normalized oscillation frequencies versus dry Ra. The solid lines show power-law fits: $0.017\,\mathrm{Ra}^{0.50}$ for dry convection and $0.689\,\mathrm{Ra}^{0.33}$ for moist and cloudy convection. The red line additionally shows the power-law fit determined by Qiu *et al.* [8] for RB convection experiments in water. The exponent for dry convection corresponds reasonably well with those determined in other RB convection experiments using different fluids such as water [8,34], helium [29,43], and mercury [30,44]. The experiments of Funfschilling and Ahlers [3] (methanol as working fluid) and Xie *et al.* [45] (water as working fluid) reported an exponent of 0.36, which is close to the exponent we obtained in our wet convection experiments.

When comparing the slopes of turbulent kinetic energy dissipation rates as a function of Ra (Fig. 6) and the slopes of the normalized oscillation frequency as a function of Ra (Fig. 10), it becomes apparent that in both cases the difference between dry and wet convection appears similar. This already hints, therefore, that these small- and large-scale properties are linked. In Fig. 11, $f_0 H^2/\kappa$ is plotted as a function of the bulk average turbulent kinetic energy dissipation rate (normalized), and we observe that the measurements, for both dry and wet convection, collapse on a single line. This strongly suggests that both the sloshing or torsional mode of the LSC and the turbulent kinetic energy

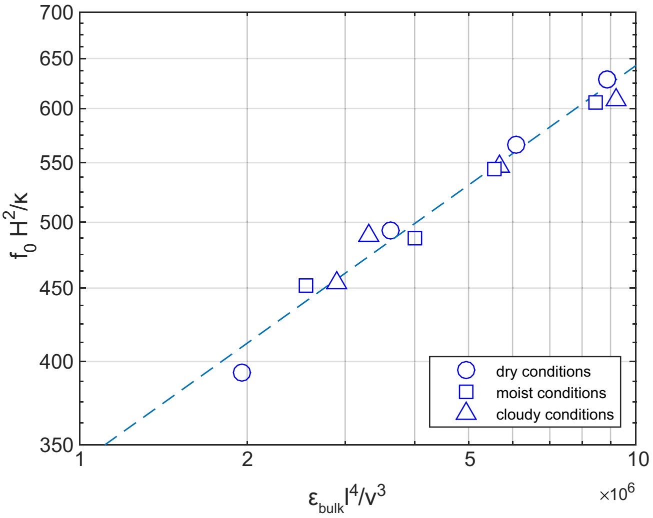

FIG. 11. Normalized oscillation frequency $f_0 H^2/\kappa$ for different temperature gradients as a function of the average turbulent kinetic energy dissipation rate in the bulk $\varepsilon_{\text{bulk}}$. A power-law fit has been applied: $f_0 H^2/\kappa \sim (\varepsilon_{\text{bulk}} l^4/\nu^3)^{0.28}$.

dissipation rate are influenced by the same mechanism. To be sure, causation cannot be determined from these data, i.e., whether LSC determines ε or the turbulent noise drives the LSC oscillations, but the collapse in scaling between the two, independently of the divergent scalings versus Ra, is convincing evidence that the two are tightly connected.

VI. SUMMARY AND CONCLUSIONS

We began by noting the growing evidence that efficiency of heat transfer in turbulent Rayleigh-Bénard convection is strongly modulated by the dynamics of an emergent LSC [3–5,7,8,37]. Recent theoretical work goes so far as to suggest that oscillations in the LSC are formally coupled to the strength (velocity) of the circulation through the nonlinear term in the Navier-Stokes equation [1,39]. Those findings would suggest that there should be a physical connection between the strength of turbulence, a small-scale property, and the characteristics of the LSC, such as its oscillation frequency.

In this study we used the Π chamber (aspect ratio $\Gamma = 2$) to investigate both the small- and large-scale flow properties of turbulent Rayleigh-Bénard convection. Experiments were carried out for Ra $\sim 10^8$–10^9 and Pr ≈ 0.7. Furthermore, experiments were run for dry, moist, and cloudy conditions. We have seen that the addition of water vapor influences the turbulent flow. In all cases, the turbulent kinetic energy dissipation rates increased with increasing temperature difference, but the slopes were different for wet and dry convection. We did not observe a clear difference between moist and cloudy convection due to low LWC. A similar lack of collapse with Ra was observed for the characteristic oscillations of the LSC. We observed that the first, normalized, characteristic oscillation frequency increased with increasing temperature difference, i.e., increasing Ra, for all conditions considered, but the slopes were different for wet and dry convection with no clear difference between moist and cloudy convection. It turned out that the sloshing or torsional mode of the LSC and the turbulent flow or kinetic energy dissipation rate seem to be influenced by the same mechanism additional to the effect of buoyancy alone. These observational results provide supporting evidence that the LSC is insensitive to phase composition or interfacial physics and rather depends only on the strength of the turbulence.

ACKNOWLEDGMENTS

We thank M. Adler for helpful comments. D.N. thanks the Alexander von Humboldt Foundation (Bonn, Germany) for fellowship support. This work was supported by the US National Science Foundation Grant No. AGS-1623429.

APPENDIX

In order to arrive at Eq. (6) we first return to the description of the buoyancy for moist convection [no condensation; see Eq. (2)], which was written in terms of virtual temperature. Using the definition of virtual temperature, the buoyancy expression can be rewritten as

$$B_v = \frac{T(1+\epsilon q_v) - T_0(1+\epsilon q_{v,0})}{T_0(1+\epsilon q_{v,0})} g. \tag{A1}$$

This equation can be simplified by computing the second-order Taylor series expansion around point $(T_0, q_{v,0})$ and using the first three terms only,

$$B_v = B_v(T_0, q_{v,0}) + (T - T_0)\partial_T B_v(T_0, q_{v,0}) + (q_v - q_{v,0})\partial_{q_v} B_v(T_0, q_{v,0}), \tag{A2}$$

where ∂_x represents the respective partial derivative. Solving this equation results in

$$B_v = \left(\frac{T - T_0}{T_0} + \frac{\epsilon(q_v - q_{v,0})}{1 + \epsilon q_v}\right) g. \tag{A3}$$

In our study $\epsilon q_v \ll 1$, $\Delta T = T - T_0$, and $\Delta q_v = q_v - q_{v,0}$, so Eq. (A3) can be written as

$$B_v = \left(\frac{\Delta T}{T_0} + \epsilon \Delta q_v\right) g. \tag{A4}$$

In analogy to [46], where the derivation of the analogous scenario of double-diffusive convection is given, we can derive Ra for moist convection (no condensation). Starting from the Boussinesq set of Navier-Stokes equations, performing the Reynolds decomposition of the total flow field, taking into account the basic state which is represented by the quiescent fluid, and dropping quadratic- and higher-order terms results in the momentum equation

$$\frac{\partial \mathbf{u}}{\partial t} = -\frac{1}{\rho_0}\nabla p + g\left(\frac{T'}{T_0} + \epsilon q_v'\right)\mathbf{k} + \nu \nabla^2 \mathbf{u}, \tag{A5}$$

where ρ_0 is the reference density. Forming the ratio of buoyant force and viscous force [i.e., the last two terms in Eq. (A5)] and setting $T' \sim \Delta T$, $q_v' \sim \Delta q_v$, $\nabla \sim 1/H$, and the vertical velocity scale $w \sim \kappa_T/H$ leads to

$$\frac{g \Delta T H^3}{T_0 \nu \kappa_T} + \frac{g \epsilon \Delta q_v H^3}{\nu \kappa_T} = \mathrm{Ra}_v. \tag{A6}$$

---

[1] G. Ahlers, S. Grossmann, and D. Lohse, Heat transfer and large scale dynamics in turbulent Rayleigh-Bénard convection, Rev. Mod. Phys. **81**, 503 (2009).

[2] F. Chillà and J. Schumacher, New perspectives in turbulent Rayleigh-Bénard convection, Eur. Phys. J. E **35**, 1 (2012).

[3] D. Funfschilling and G. Ahlers, Plume Motion and Large-Scale Circulation in a Cylindrical Rayleigh-Bénard cell, Phys. Rev. Lett. **92**, 194502 (2004).

[4] C. Sun, H.-D. Xi, and K.-Q. Xia, Azimuthal Symmetry, Flow Dynamics, and Heat Transport in Turbulent Thermal Convection in a Cylinder with an Aspect Ratio of 0.5, Phys. Rev. Lett. **95**, 074502 (2005).

[5] E. P. van der Poel, R. J. A. M. Stevens, and D. Lohse, Connecting flow structures and heat flux in turbulent Rayleigh-Bénard convection, Phys. Rev. E **84**, 045303 (2011).

[6] G. Ahlers, Trend: turbulent convection, Physics **2**, 74 (2009).

[7] H.-D. Xi, S.-Q. Zhou, Q. Zhou, T.-S. Chan, and K.-Q. Xia, Origin of the Temperature Oscillation in Turbulent Thermal Convection, Phys. Rev. Lett. **102**, 044503 (2009).

[8] X.-L. Qiu, X.-D. Shang, P. Tong, and K.-Q. Xia, Velocity oscillations in turbulent Rayleigh-Bénard convection, Phys. Fluids **16**, 412 (2004).

[9] H. Siebert, H. Franke, K. Lehmann, R. Maser, E. W. Saw, R. A. Shaw, D. Schell, and M. Wendisch, Probing finescale dynamics and microphysics of clouds with helicopter-borne measurements, Bull. Am. Meteorol. Soc. **87**, 1727 (2006).

[10] R. A. Shaw, Particle-turbulence interactions in atmospheric clouds, Annu. Rev. Fluid Mech. **35**, 183 (2003).

[11] S. P. Malinowski, M. Andrejczuk, W. W. Grabowski, P. Korczyk, T. A. Kowalewski, and P. K. Smolarkiewicz, Laboratory and modeling studies of cloud-clear air interfacial mixing: Anisotropy of small-scale turbulence due to evaporative cooling, New J. Phys. **10**, 075020 (2008).

[12] K. Chang, J. Bench, M. Brege, W. Cantrell, K. Chandrakar, D. Ciochetto, C. Mazzoleni, L. Mazzoleni, D. Niedermeier, and R. Shaw, A laboratory facility to study gas-aerosol-cloud interactions in a turbulent environment: The Π chamber, Bull. Am. Meteorol. Soc. **97**, 2344 (2016).

[13] D. Lamb and J. Verlinde, *Physics and Chemistry of Clouds* (Cambridge University Press, Cambridge, 2011), p. 231ff.

[14] A. Betts, Non-precipitating cumulus convection and its parameterization, Q. J. R. Meteorol. Soc. **99**, 178 (1973).

[15] J. W. Deardorff, Usefulness of liquid-water potential temperature in a shallow-cloud model, J. Appl. Meteor. **15**, 98 (1976).

[16] G.-W. He and J.-B. Zhang, Elliptic model for space-time correlations in turbulent shear flows, Phys. Rev. E **73**, 055303 (2006).

[17] X. He, G.-W. He, and P. Tong, Small-scale turbulent fluctuations beyond Taylor's frozen-flow hypothesis, Phys. Rev. E **81**, 065303(R) (2010).

[18] X. He, D. P. van Gils, E. Bodenschatz, and G. Ahlers, Reynolds numbers and the elliptic approximation near the ultimate state of turbulent Rayleigh-Bénard convection, New J. Phys. **17**, 063028 (2015).

[19] H. Tennekes and J. L. Lumley, *A First Course in Turbulence* (MIT Press, Cambridge, 1999).

[20] S. Chen and R. H. Kraichnan, Sweeping decorrelation in isotropic turbulence, Phys. Fluids A **1**, 2019 (1989).

[21] K. P. Iyer and P. K. Yeung, Structure functions and applicability of Yaglom's relation in passive-scalar turbulent mixing at low Schmidt numbers with uniform mean gradient, Phys. Fluids **26**, 085107 (2014).

[22] K. R. Sreenivasan, The passive scalar spectrum and the Obukhov-Corrsin constant, Phys. Fluids **8**, 189 (1996).

[23] J. D. Scheel and J. Schumacher, Predicting transition ranges to fully turbulent viscous boundary layers in low Prandtl number convection flows, Phys. Rev. Fluids **2**, 123501 (2017).

[24] S. Grossmann and D. Lohse, Scaling in thermal convection: a unifying theory, J. Fluid Mech. **407**, 27 (2000).

[25] S. Grossmann and D. Lohse, Thermal Convection for Large Prandtl Numbers, Phys. Rev. Lett. **86**, 3316 (2001).

[26] S. Grossmann and D. Lohse, Prandtl and Rayleigh number dependence of the Reynolds number in turbulent thermal convection, Phys. Rev. E **66**, 016305 (2002).

[27] S. Grossmann and D. Lohse, Fluctuations in turbulent Rayleigh-Bénard convection: The role of plumes, Phys. Fluids **16**, 4462 (2004).

[28] F. Heslot, B. Castaing, and A. Libchaber, Transitions to turbulence in helium gas, Phys. Rev. A **36**, 5870(R) (1987).

[29] B. Castaing, G. Gunaratne, F. Heslot, L. Kadanoff, A. Libchaber, S. Thomae, X.-Z. Wu, S. Zaleski, and G. Zanetti, Scaling of hard thermal turbulence in Rayleigh-Bénard convection, J. Fluid Mech. **204**, 1 (1989).

[30] S. Cioni, S. Ciliberto, and J. Sommeria, Strongly turbulent Rayleigh-Bénard convection in mercury: Comparison with results at moderate Prandtl number, J. Fluid Mech. **335**, 111 (1997).

[31] X.-L. Qiu, S.-H. Yao, and P. Tong, Large-scale coherent rotation and oscillation in turbulent thermal convection, Phys. Rev. E **61**, 6075(R) (2000).

[32] X.-L. Qiu and P. Tong, Temperature oscillations in turbulent Rayleigh-Bénard convection, Phys. Rev. E **66**, 026308 (2002).

[33] J. J. Niemela, L. Skrbek, K. R. Sreenivasan, and R. J. Donnelly, Turbulent convection at very high Rayleigh numbers, J. Fluid Mech. **449**, 169 (2001).

[34] X.-L. Qiu and P. Tong, Onset of Coherent Oscillations in Turbulent Rayleigh-Bénard Convection, Phys. Rev. Lett. **87**, 094501 (2001).

[35] K. R. Sreenivasan, A. Bershadskii, and J. J. Niemela, Mean wind and its reversal in thermal convection, Phys. Rev. E **65**, 056306 (2002).

[36] C. Resagk, R. du Puit, A. Thess, F. V. Dolzhansky, S. Grossmann, F. F. Araujo, and D. Lohse, Oscillations of the large scale wind in turbulent thermal convection, Phys. Fluids **18**, 095105 (2006).

[37] D. Funfschilling, E. Brown, and G. Ahlers, Torsional oscillations of the large-scale circulation in turbulent Rayleigh-Bénard convection, J. Fluid Mech. **607**, 119 (2008).

[38] N. Shi, M. S. Emran, and J. Schumacher, Boundary layer structure in turbulent Rayleigh-Bénard convection, J. Fluid Mech. **706**, 5 (2012).

[39] E. Brown and G. Ahlers, The origin of oscillations of the large-scale circulation of turbulent Rayleigh-Bénard convection, J. Fluid Mech. **638**, 383 (2009).

[40] T. Hayakawa and Y. Tsuji, Mean wind: Its velocity and temperature fluctuation in low-Prandtl-number thermal convection, Physica D **239**, 1353 (2010).

[41] J. Bjerknes, Saturated-adiabatic ascent of air through dry-adiabatically descending environment, Q. J. R. Meteorol. Soc. **64**, 325 (1938).

[42] J. Schumacher and O. Paulius, Buoyancy statistics in moist turbulent Rayleigh-Bénard convection, J. Fluid Mech. **648**, 509 (2010).

[43] X. Chavanne, F. Chilla, B. Castaing, B. Hebral, B. Chabaud, and J. Chaussy, Observation of the Ultimate Regime in Rayleigh-Bénard Convection, Phys. Rev. Lett. **79**, 3648 (1997).

[44] J. Schumacher, V. Bandaru, A. Pandey, and J. D. Scheel, Transitional boundary layers in low-Prandtl-number convection, Phys. Rev. Fluids **1**, 084402 (2016).

[45] Y.-C. Xie, P. Wei, and K.-Q. Xia, Dynamics of the large-scale circulation in high-Prandtl-number turbulent thermal convection, J. Fluid Mech. **717**, 322 (2013).

[46] P. K. Kundu, I. M. Cohen, and D.-R. Dowling, *Fluid Mechanics*, 6th ed. (Academic, New York, 2016).